Title
Measurements, modelling and electron cyclotron heating modification of Alfvén eigenmode activity in DIII-D

Journal
Nuclear Fusion, 49(6)

ISSN
0029-5515

Authors
Van Zeeland, MA
Heidbrink, WW
Nazikian, R
et al.

Publication Date
2009-06-01

DOI
10.1088/0029-5515/49/6/065003

Nucl. Fusion **49** (2009) 065003 (13pp) doi:10.1088/0029-5515/49/6/065003

Measurements, modelling and electron cyclotron heating modification of Alfvén eigenmode activity in DIII-D

M.A. Van Zeeland[1], W.W. Heidbrink[2], R. Nazikian[3], M.E. Austin[4], C.Z. Cheng[5], M.S. Chu[1], N.N. Gorelenkov[3], C.T. Holcomb[6], A.W. Hyatt[1], G.J. Kramer[3], J. Lohr[1], G.R. McKee[7], C.C. Petty[1], R. Prater[1], W.M. Solomon[3] and D.A. Spong[8]

[1] General Atomics, PO Box 85608 San Diego, CA 92186-5608, USA
[2] Department of Physics and Astronomy, University of California-Irvine, Irvine, CA, USA
[3] Princeton Plasma Physics Laboratory, Princeton, NJ, USA
[4] Institute for Fusion Studies, University of Texas-Austin, Austin, TX, USA
[5] Plasma and Space Science Center, National Cheng Kung University, Tainan, Taiwan, Republic of China
[6] Lawrence Livermore National Laboratory, Livermore, CA, USA
[7] Department of Engineering Physics, University of Wisconsin-Madison, Madison, WI, USA
[8] Oak Ridge National Laboratory, Oak Ridge, TN, USA

E-mail: vanzeeland@fusion.gat.com

Received 12 January 2009, accepted for publication 31 March 2009
Published 30 April 2009
Online at stacks.iop.org/NF/49/065003

Abstract
Neutral beam injection into reversed magnetic shear DIII-D plasmas produces a variety of Alfvénic activity including toroidicity and ellipticity induced Alfvén eigenmodes (TAE/EAE, respectively) and reversed shear Alfvén eigenmodes (RSAE) as well as their spatial coupling. These modes are studied during the discharge current ramp phase when incomplete current penetration results in a high central safety factor and strong drive due to multiple higher order resonances. It is found that ideal MHD modelling of eigenmode spectral evolution, coupling and structure are in excellent agreement with experimental measurements. It is also found that higher radial envelope harmonic RSAEs are clearly observed and agree with modelling. Some discrepancies with modelling such as that due to up/down eigenmode asymmetries are also pointed out. Concomitant with the Alfvénic activity, fast ion (FIDA) spectroscopy shows large reductions in the central fast ion profile, the degree of which depends on the Alfvén eigenmode amplitude. Interestingly, localized electron cyclotron heating (ECH) near the mode location stabilizes RSAE activity and results in significantly improved fast ion confinement relative to discharges with ECH deposition on axis. In these discharges, RSAE activity is suppressed when ECH is deposited near the radius of the shear reversal point and enhanced with deposition near the axis. The sensitivity of this effect to deposition power and current drive phasing as well as ECH modulation are presented.

PACS numbers: 52.35.Py, 52.35.Bj, 52.55.Fa, 52.70.Ds, 52.30.Cv, 52.65.Kj

(Some figures in this article are in colour only in the electronic version)

1. Introduction

Future burning plasma experiments such as ITER may be subject to the excitation of Alfvén eigenmode (AE) instabilities by 3.5 MeV fusion born alpha particles needed to sustain the thermonuclear burn as well as neutral beam ions critical for heating, current drive and momentum input [1–3]. If allowed to grow unabated, these instabilities have the potential to cause fast ion redistribution or loss and possible damage to first wall components [4]. Consequently, developing validated predictive models for this nonlinear interaction as well as control techniques to suppress these instabilities is critical for extrapolating to ITER and beyond. Recent experimental results from the DIII-D tokamak have validated several key elements of AE theory including the linear coupling of multiple AEs [5, 6], excitation of AEs by sub-Alfvénic beam ions via higher order passing ion resonances at low-n [7], passing thermal ion resonances at high-n [8]

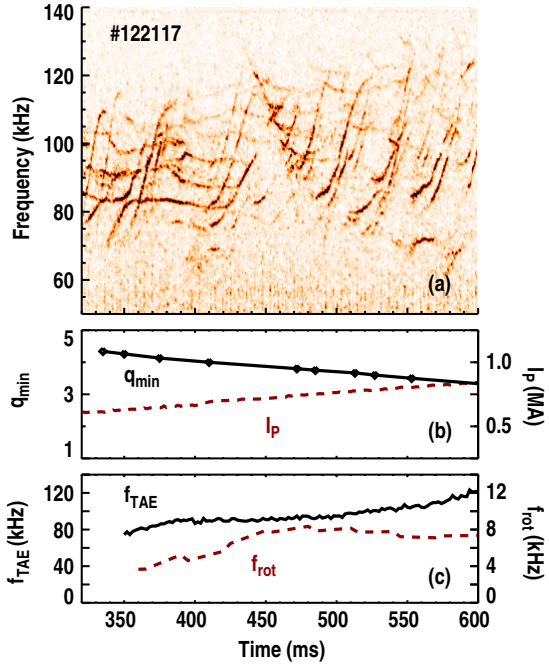

Figure 1. Data from DIII-D discharge 122117. (*a*) Power spectrum of a vertical CO_2 interferometer chord and BES channel near q_{min}. (*b*) q_{min} evolution inferred from RSAEs (diamonds) and MSE (solid), plasma current (dashed). (*c*) TAE frequency (solid) and toroidal rotation frequency (dashed) at q_{min}.

and spatial eigenmode structure of various AEs in reversed magnetic shear plasmas [6, 9]. These studies have also yielded several surprising findings. First, localized electron cyclotron heating (ECH) near the mode location stabilized reversed shear Alfvén eigenmodes RSAEs [10] and results in significantly improved fast ion confinement relative to similar discharges with ECH deposition on axis [11]. Second, detailed orbit-following simulations using multiple experimentally validated eigenmodes fail to reproduce the large measured fast ion deficit [12, 13].

This paper discusses recent results on MHD modelling of AE measurements in DIII-D where comparison is made with eigenmode spectral evolution, coupling and structure. Details of eigenmode structure including higher radial envelope harmonic RSAEs are clearly observed and agree with modelling. Some discrepancies with modelling such as that due to up/down eigenmode asymmetries are also found. Following the presentation of eigenmode modelling and measurements, we summarize the observed suppression of RSAEs by localized ECH injection and present experimental results related to the sensitivity of this effect to deposition power and current drive phasing as well as ECH modulation.

2. Measurements and modelling of Alfvén eigenmodes

The primary discharges of interest in this study are analysed during the current ramp phase (figure 1(*b*)) when 5 MW, 78 kV, unbalanced co-going, sub-Alfvénic ($V_B/V_A \approx 0.4$), neutral deuterium beams are injected into the plasma. The central β (plasma pressure/magnetic field pressure) is increasing during this period, and there is an off-axis minimum in the magnetic safety factor (q_{min}). The electron density is relatively low ($n_e \approx 2 \times 10^{13}\,cm^{-3}$), and the fast ion pressure is roughly half of the total plasma pressure according to TRANSP [14] analysis. Several fluctuation diagnostics indicate a variety of Alfvénic activity in this discharge. Shown in figure 1(*a*) is a crosspower spectrum of a beam emission spectroscopy (BES) channel located near q_{min} and a vertical CO_2 interferometer chord [15]. Previous analysis has identified the modes chirping up in frequency as RSAEs [10] and the series of relatively constant frequency modes as TAEs [6, 9] (for reference, the TAE frequency at q_{min} is plotted in figure 1(*c*) as well as the charge exchange recombination measured toroidal rotation frequency at q_{min}). Over the time window shown, the RSAE spectral behaviour is typical for q_{min} decreasing with an integer crossing ($q_{min} = 4$) at approximately $t = 410$ ms [9, 16, 19]. Plotted in figure 1(*b*) (solid-diamonds) are values of q_{min} derived from the RSAE activity [19] in combination with motional Stark effect (MSE) measurements [20].

2.1. Eigenmode spectral evolution and structure

Precise knowledge of the q_{min} evolution made possible through RSAE identification is fundamental to the recently reported progress in AE modelling using the ideal MHD code NOVA [9, 17, 18, 21, 22]. An example of the NOVA calculated eigenfrequencies for a subset of figure 1(*a*) is shown in figure 2(*b*), where $n = 2$–4 RSAEs and two $n = 3$ TAEs are identified and excellent agreement with the experimentally measured spectral evolution (figure 2(*a*)) is shown. The NOVA modelling is shown as a function of q_{min} to further convey how small changes in q_{min} ($\delta q_{min}/q_{min} \approx 5\%$) completely determine the modelling results—essentially all other parameters are playing little to no role in the spectral variation during the interval shown. The occasional gaps in the experimentally observed mode amplitudes and frequency evolution, such as that appearing at approximately $t = 352$ ms, $f = 83$ kHz are a signature of mode–mode coupling and have been investigated in detail recently [5, 6]. It was found this particular gap was formed by the coupling of an RSAE and global TAE, behaviour which is reproduced by the NOVA modelling near $q_{min} = 4.23$. Throughout the coupling process, the calculated spatial eigenmodes are linear odd/even parity combinations of the two original eigenmodes, a process that has been verified by comparison with electron cyclotron emission (ECE) measurements [6].

A comparison of the NOVA calculated eigenmode with ECE data is shown in figure 3(*a*) for the $f = 78$ kHz TAE from figure 2(*b*), where the perturbed electron temperature (δT_e) is plotted versus the normalized square root of toroidal flux (ρ). For comparison with ECE measurements, a synthetic diagnostic as described in [9] was used to process the NOVA predicted temperature perturbation. The actual poloidal harmonic content/structure comprising the TAE is shown in figure 2(*b*), where it is seen that at least 10 harmonics contribute significantly, something typical of the global TAEs discussed here. By scaling the NOVA prediction using a single constant to match the ECE data (figure 3(*a*)) the amplitude of the perturbation wavefields is obtained. The inferred amplitude is shown in figure 3(*c*) as a function of major radius (R) along the device midplane, where the radial magnetic field perturbation

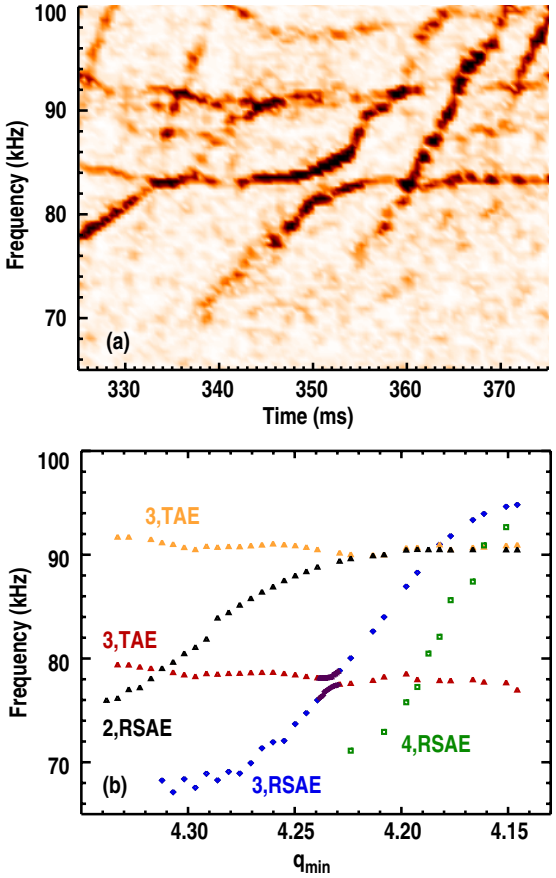

Figure 2. (*a*) Enlarged region of figure 1(*a*). (*b*) NOVA modelling for $q_{\min}$ range of panel (*a*) showing calculated frequencies for several RSAEs and TAEs. Modes are identified with toroidal mode number followed by type of eigenmode.

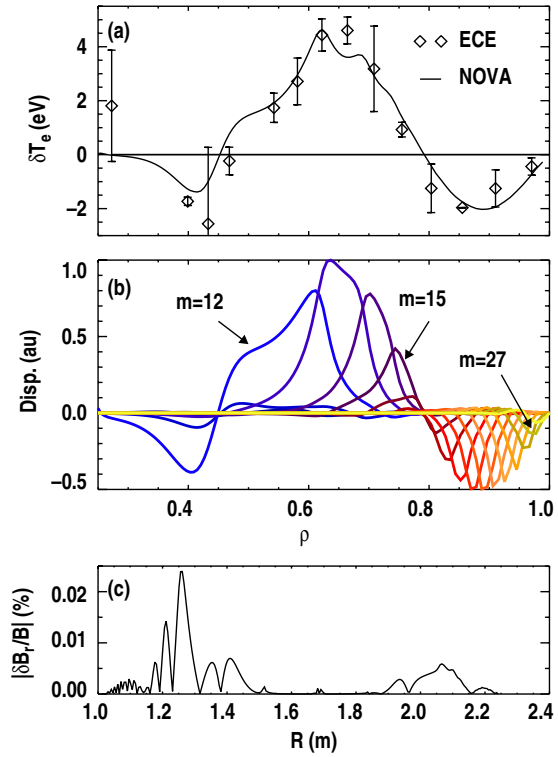

Figure 3. (*a*) Synthetic ECE diagnostic prediction (solid) using NOVA calculated $f = 78$ kHz global TAE from figure 2 overlayed with ECE measurements (diamonds). NOVA prediction scaled by single constant to match ECE data. (*b*) Poloidal harmonics comprising TAE from panel (*a*). (*c*) Calculated radial component of magnetic field fluctuation along device midplane (versus major radius) using amplitude obtained from comparison with ECE data.

(δB_r) is scaled to the local magnetic field strength $|B|$. For the majority of experiments on DIII-D, typically AE amplitudes obtained in this manner are found to be $\delta B_r/B < 10^{-3}$. This perturbed field amplitude combined with the poloidal harmonic structure (figure 3(*b*)) has been used to form the input eigenmodes for fast ion transport modelling such as that discussed in [12, 13].

While the RSAE activity during the earlier phase ($t < 450$ ms) of figure 1 can be described well by only a single RSAE for each n at any given time, often it is the case that multiple sets of up-sweeping RSAEs appear to be superimposed on each other. Such a case is shown in figure 4(*a*), where a windowed power spectrum of BES data for a later time range of the same discharge as figure 1 is given and two $n = 4$ RSAEs (labelled RSAE-1 and RSAE-2) are pointed out. There are two possible explanations for the simultaneous existence of two up-chirping, same n, similar frequency (i.e. not nonlinear harmonics) RSAEs in a given discharge. The first is due to multiple minima in the q-profile, which is not the case here, and the second is that these eigenmodes are radial harmonics of the fundamental RSAE. By radial harmonic, it is meant that the radial eigenmode envelope has an increasing number of nodes given by the integer l, where the fundamental has $l = 0$ [23]. The measured radial structure of the two eigenmodes is shown in figures 4(*b*)–(*d*), where the amplitude (δT_e), phase relative to the peak location (ϕ), and $\delta T_e \cos(\phi)$ are plotted respectively. The higher frequency mode is the typical RSAE and the mode labelled RSAE-2 is the first radial harmonic with a radial node near the peak of the RSAE-1, something made apparent in figure 4(*d*). The radial phase structure shows a flat phase profile across the peak of RSAE-1 and as expected, a clear 180° phase inversion at the middle of RSAE-2 near $\rho = 0.4$. Both eigenmodes are centred at $q_{\min}$ (see overlayed q-profile) a characteristic of RSAEs [24]. Outside of $\rho \approx 0.6$, both eigenmodes also appear to be coupled slightly to global TAEs which accounts for the additional radial structure and will be further explained by NOVA modelling [19].

The measured RSAEs are anti-Sturmian with the higher radial harmonics decreasing in frequency as theoretically expected and predicted by the NOVA code [23]. NOVA calculations for the experimental parameters of figure 4 are shown in figure 5, where the $n = 4$ Alfvén continuum is given (figure 5(*a*)) along with the radial structure of several RSAEs (figures 5(*b*)–(*e*)). The eigenmode displacement in figures 5(*b*)–(*e*) is shown for 21 poloidal harmonics ($m = 10$–30) and in each case the eigenmode shape is predominantly determined by the structure of a single harmonic, $m = 14$ (shown in black). This single dominant poloidal harmonic is another characteristic of RSAEs and is expected for $n = 4$ eigenmodes given $q_{\min} = 3.45 \approx 14/4$. The $l = 0$ and $l = 1$ eigenmodes (figures 5(*b*)–(*c*)) correspond to those observed experimentally (figure 4). In addition to the

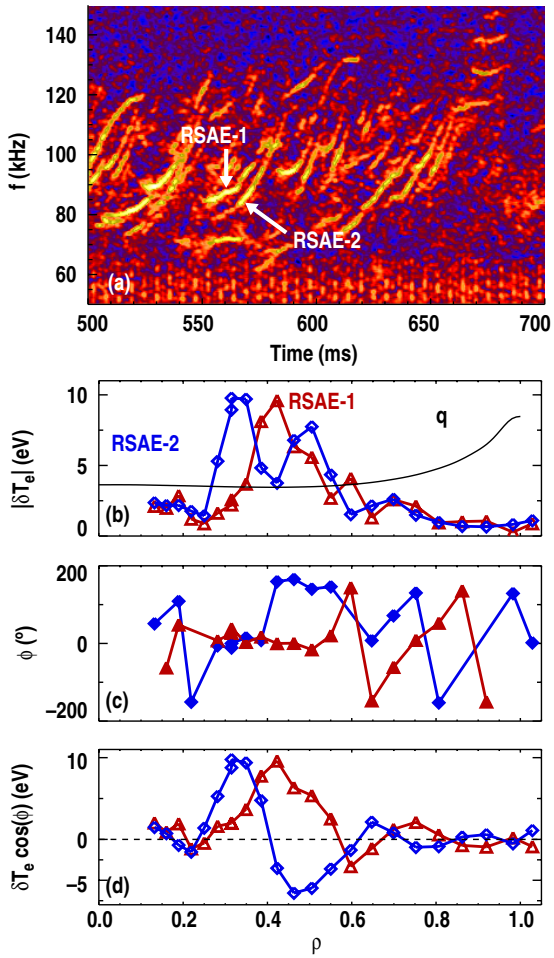

Figure 4. Discharge 122117. (*a*) Crosspower spectrum of adjacent BES channels near $q_{\min}$. (*b*) ECE measured temperature perturbation amplitude (δT_e) for modes labelled RSAE-1 and RSAE-2 in panel (*a*). q-profile overlayed. (*c*) Phase (ϕ) structure of eigenmodes where phase is defined relative to peak amplitude channel. (*d*) $\delta T_e \cos(\phi)$.

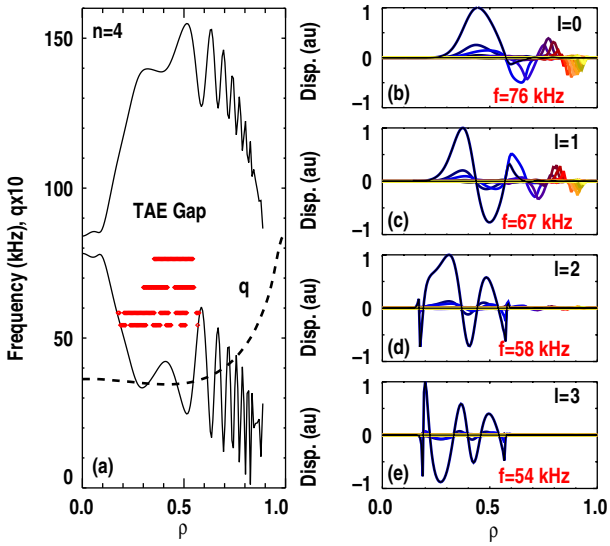

Figure 5. NOVA modelling of discharge 122117 data in figure 4. (*a*) $n = 4$ Alfvén continuum, RSAE frequencies are plotted where eigenmode displacement is above 35% of peak value (red). (*b*)–(*e*) Displacement radial structure of $m = 10$–30 harmonics for RSAEs found by NOVA. $m = 14$ harmonic is black. Eigenfrequency as well as order of radial envelope (l) is labelled.

radial nodes, it is also seen that the modelling captures several of the other detailed experimental features, for example, both the $l = 0$ and $l = 1$ NOVA calculated eigenmodes have additional radial structure outside of $\rho \approx 0.6$ due to coupling with global TAEs, as observed experimentally. The global TAEs participating in the coupling are composed of many poloidal harmonics similar to the one presented in figure 3. As a further point of comparison, the eigenmodes are all centred near $q_{\min}$ and the Alfvén continuum accumulation point as can be seen in figure 5(*a*) where each of the NOVA calculated $l = 0$–3 eigenmode frequencies is plotted over the Alfvén continuum at the radial locations where its displacement is above 0.35. When adjusted for Doppler shifts ($\delta f_{\text{Doppler}} = nf_{\text{rot}}$), the calculated frequencies are also in agreement with experimental measurements $f_1 = 76 + 4 \times 4 = 92$ kHz and $f_2 = 67 + 4 \times 4 = 83$ kHz from NOVA to be compared with $f_1 = 92$ and $f_2 = 84$ kHz experimentally (at $t = 566.8$ ms), where a 4 kHz rotation frequency at $q_{\min}$ has been used. Unadjusted for Doppler shift, the difference in frequencies between the $l = 0$ and $l = 1$ mode can be compared and is also essentially equal to that observed within the experimental uncertainties.

When each of the $l = 0$–3 eigenmodes is compared with its location with respect to the Alfvén continuum it becomes obvious why the upper two eigenmodes are able to couple to global TAEs (several of which are present but not plotted). The $l = 0$ and $l = 1$ eigenmodes are above the local continuum and not bounded by the well created between the $q = (m - 1/2)/n$ and $q = (m + 1/2)/n$ surfaces, while the $l = 2$ and $l = 3$ eigenmodes are. This fact can be seen in the displacement plots of figures 5(*d*) and (*e*) where the edges of the $l = 2$ and $l = 3$ eigenmodes terminate in a spiky behaviour characteristic of an interaction with the continuum. Indeed, this interaction may be the reason these higher harmonics are not observed experimentally.

As mentioned above, in figure 4(*c*), the radial eigenmode phase structure is as expected over the bulk of the RSAE eigenfunctions, however, at radii outside of $\rho \approx 0.6$, where the eigenmodes are coupled to global TAEs, the phase of the mode relative to the peak location appears to be changing rapidly with increasing radius. As another example of this point, figure 6 shows the measured radial δT_e structure due to a global TAE in the same discharge. The eigenmode phase structure [$\phi(\rho)$] shown in panel 6(*b*) clearly has a radially increasing phase until $\rho \approx 0.8$, where the phase has a 2π phase inversion due to the fact that it is only defined over the interval $-\pi$ to π. Shown in figure 6(*c*) is the coherence of each channel relative to the peak channel and channels above the 95% confidence level are highlighted to indicate which ones are reliably seeing the eigenmode [25]. Radially ramping $\phi(\rho)$ such as this is often observed when looking at global TAEs as opposed to modes such as the RSAE which is composed of relatively few poloidal harmonics. This particular eigenmode corresponds to the higher frequency $n = 3$ TAE in figure 2. On the device midplane, where the ECE radiometer measures, NOVA is not capable of predicting a phase structure such as this. The NOVA code assumes an up/down symmetric equilibrium

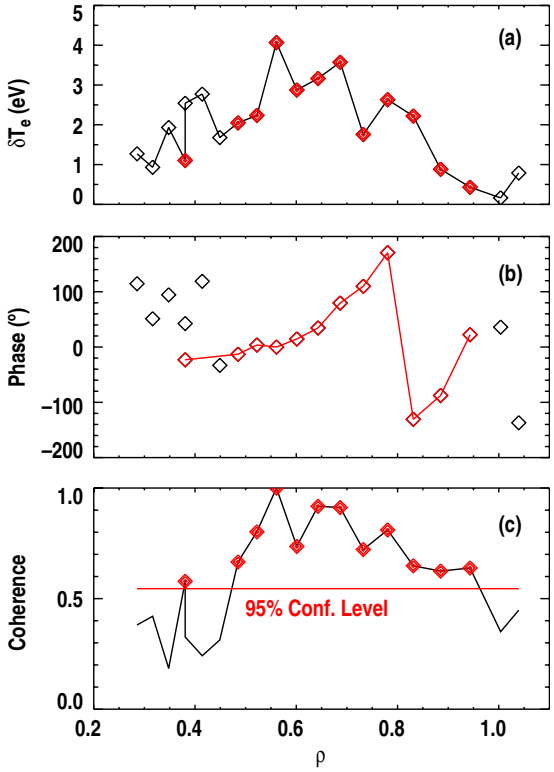

Figure 6. Discharge 122117, ECE data at $t = 341.75$ ms, $f = 90.82$ kHz, representing global TAE plotted in figure 2. (*a*) Eigenmode amplitude, (*b*) Eigenmode phase relative to peak channel. (*c*) Coherence relative to peak channel. Channels with coherence above 95% confidence level plotted in red.

and eigenmode structure, a consequence of which is a radial eigenmode phase at $z = 0$ that is either $\phi = 0$ or $\phi = \pi$ with respect to the peak location along the midplane. A radially ramping phase structure like that in figure 6(*b*) is inconsistent with NOVA calculations and results in an eigenmode that appears to be 'twisted' at a given poloidal cross-section rather than up/down symmetric.

Several other MHD solvers are able to handle up/down asymmetric eigenmodes, one example of which is TAEFL which is an initial value reduced MHD/gyrofluid code [26–28]. TAEFL has been employed previously to study AEs in DIII-D and was initialized for this study using the same input profiles as the NOVA modelling presented in figure 2(*b*). TAEFL finds the fastest growing linear eigenmode for a given toroidal mode number, where the fast ions providing the drive are also included self-consistently in the eigenmode calculation. The fast ion pressure profile used as an input was obtained by subtraction of the thermal pressure profile from the EFIT equilibrium profile [29]. The TAEFL calculated eigenmode, using the experimental profiles, is shown in figure 7 where the 2D potential structure is shown in figure 7(*a*) and the phase and amplitude along the outboard midplane are given in figures 7(*b*) and (*c*) respectively. As colloquially stated above, this eigenmode appears to be 'twisted' in the poloidal cross-section, whereas the equivalent NOVA eigenmode would be up/down symmetric (an example of which is given in the following section in figure 9). When Fourier analysed, this eigenmode indeed has a phase structure (figure 7(*b*)) very

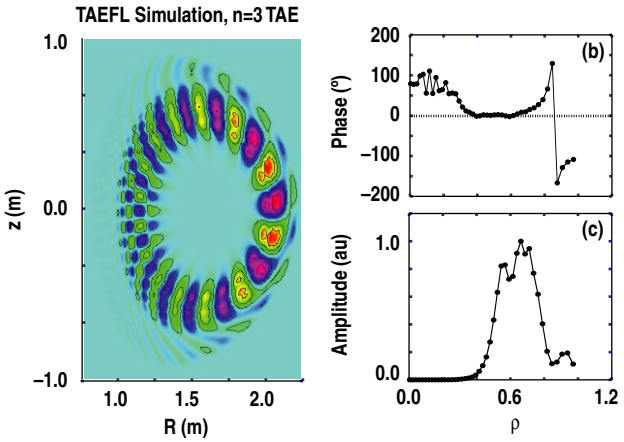

Figure 7. TAEFL modelling of discharge 122117 at $t = 341$ ms. (*a*) 2D $n = 3$ TAE structure, contours of potential are shown (red positive, black negative). (*b*) Eigenmode phase across outboard midplane. (*c*) Eigenmode potential amplitude.

similar to that observed experimentally (figure 6(*b*)), i.e. it ramps up radially. Experimentally, this type of phase variation can be due to a variety of effects including toroidal rotation, up/down asymmetric equilibria, and diamagnetic flows (ω_* effects); the latter of which is responsible for the structure in TAEFL since rotation is not included for this study and the actual equilibrium is assumed to be up/down symmetric.

One practical consequence of this asymmetric phase structure is the effect it has on line-integrated measurements. While the local perturbed field amplitude (δn_e or δT_e) may not be changed significantly, line-integrals through the perturbed 3D fields, such as those measured by x-ray detection and interferometery, can be radically different. Perfectly symmetric eigenmodes are more prone to cancellation of line-integrated perturbations and when synthetic line-integrated diagnostics are applied to symmetric eigenmodes such as those in NOVA this should be considered. In general, while assuming up/down symmetric eigenmodes and plasmas can reproduce many of the experimental features, to fully capture the dynamics, up/down asymmetry must be included in AE modelling.

2.2. *Eigenmode drive*

In a first step towards understanding the interaction of the observed AE with the fast ion population, a linear stability analysis is carried out using the NOVA-K code [30, 31]. This code uses the ideal MHD eigenmode solutions generated by NOVA and calculates the drive and damping using a perturbative procedure incorporating the fast ion distribution through an analytic approximation to TRANSP analysis. Figure 8(*a*) displays a plot of the analytical beam ion distribution generated for beam ions in the plasma of figure 1 at $t = 359$ ms. The overplotted solid lines represent boundaries for different classes of orbits. The colour surface plot represents beam ion density at one-half the injection energy plotted versus normalized fast ion invariants of the motion, $\lambda = \chi^2 R/R_o$ and P_ξ/Ψ_W, where $\chi = V_\perp/V_b$, $P_\xi = V_\parallel B_o/B - \Psi_{pol}(r)$ is the canonical momentum, $\Psi_{pol}(r)$ is the poloidal magnetic flux at minor radius r, Ψ_W is the poloidal

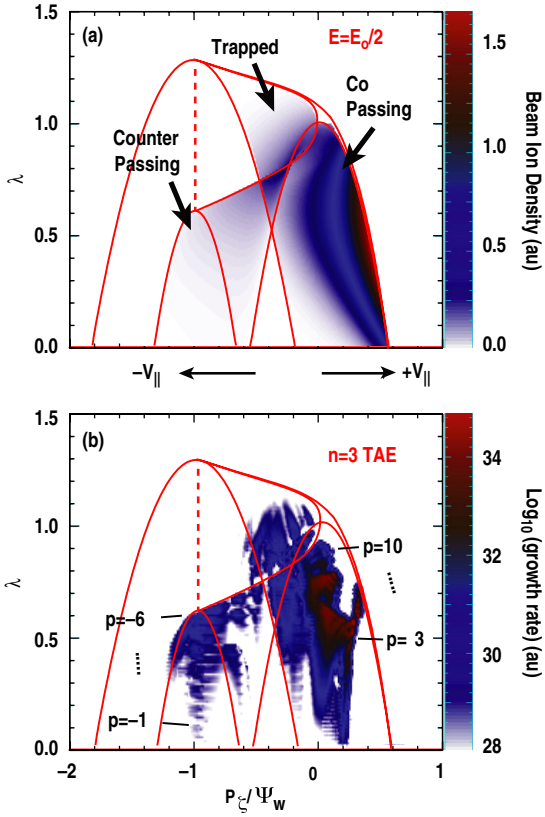

Figure 8. (*a*) Analytic model based on TRANSP results for 40 keV ion distribution function in 122117 at = 359 ms. Solid red curves represent boundaries for different classes of orbits [4]. Potato orbits occur at the intersection between trapped and co-passing boundaries. (*b*) NOVA-K calculated drive integrated over all energies for TAE of figure 3. Range of resonance orders (p) labelled.

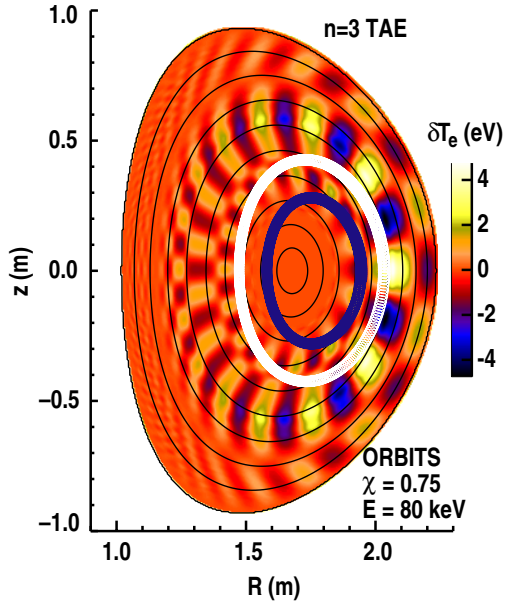

Figure 9. 2D structure of NOVA calculated $n = 3$ TAE temperature perturbation from figure 3 using scaling constant derived from ECE data. Overlayed black contours are ρ. White and blue curves are fast ion orbit trajectories initialized on outboard plasma midplane near $q_{\min}$ and mode peak respectively. Both ions are co-passing 80 keV with pitch 0.75 (near peak in distribution function).

flux at the last closed flux surface, B is the local magnetic field strength, B_o is the magnetic field strength on the magnetic axis [7]. In figure 8(*a*) the majority of beam ions are deposited in a relatively small region of velocity space that is comprised primarily of co-passing particles. Physically, the axes can be explained as follows. Moving up the vertical axis, the pitch angle of the particle relative to the magnetic field line increases so particles are deeply passing at low values of the vertical axis and deeply trapped at the upper range. Along the horizontal axis, particles are moving in the direction counter to the plasma current to the far left and move in the direction of the plasma current towards the right, with an offset determined by the magnetic flux at the particle location [7].

Figure 8(*b*) shows the calculated drive integrated over all energies for the TAE of figure 3, and allows one to dissect the regions of velocity space that interact with the eigenmode. From this plot it is immediately clear that a large fraction of the fast ion population can contribute to the drive for this mode. The boundaries shown are approximate and only strictly correct for 40 keV, however, it can be seen that the dominant drive is coming from co-passing particles (axis encircling passing particles near the injection pitch angle contribute approximately 95% of the mode drive) and perhaps surprisingly, some drive is coming from the counter passing particles. Potato orbits (intersection between trapped and co-passing boundary in figure 8(*a*)) also contribute to mode drive, however relative to the other classes of orbits, the number of particles in potato orbits is small and the integrated drive from these particles is very weak. More precisely, this analysis identifies the role of higher order passing resonances in the mode excitation where the resonance order p is defined according to the standard passing particle resonance condition given by

$$\omega - n\omega_{\rm pr} - [(m - nq) + p]\omega_\theta = 0, \qquad (1)$$

where ω_θ is the poloidal transit frequency, ω is the mode frequency, p is a nonzero positive or negative integer, and $\omega_{\rm pr}$ is the particle toroidal precession frequency [7, 32]. Physically, this equation is equivalent to the statement that when a resonant particle makes a full transit in the poloidal angle, the phase of the wave with poloidal/toroidal mode numbers at the particle should change by a multiple of 2π [33]. Again, in interpreting figure 8(*b*), the initial particle distribution must be considered since it is convolved with the relative strength of each resonance.

The relative strength of the drive for a given p is a strong function of the discharge equilibrium. The fundamental ($p = \pm 1$) resonance represents the strongest channel for wave particle interaction, when $m\rho_{\rm FI}/r \ll 1$; however, at high q as in these discharges, $m\rho_{\rm FI}/r \approx 1$, where $\rho_{\rm FI}$ is the fast ion gyroradius and r is the minor radius. High $q_{\min}$ reversed shear plasmas such as these lead to significant higher order resonant drive since the particle poloidal trajectory exhibits large deviations from flux surfaces, particularly near the magnetic axis where the poloidal field is relatively small [7, 34]. This can be seen in figure 9, where the trajectories of two fast ions with the injection energy of 80 keV and $V_\|/|V| = 0.75$ are plotted along with contours of toroidal flux and coloured contours of the temperature perturbation structure due to the $n = 3$ TAE

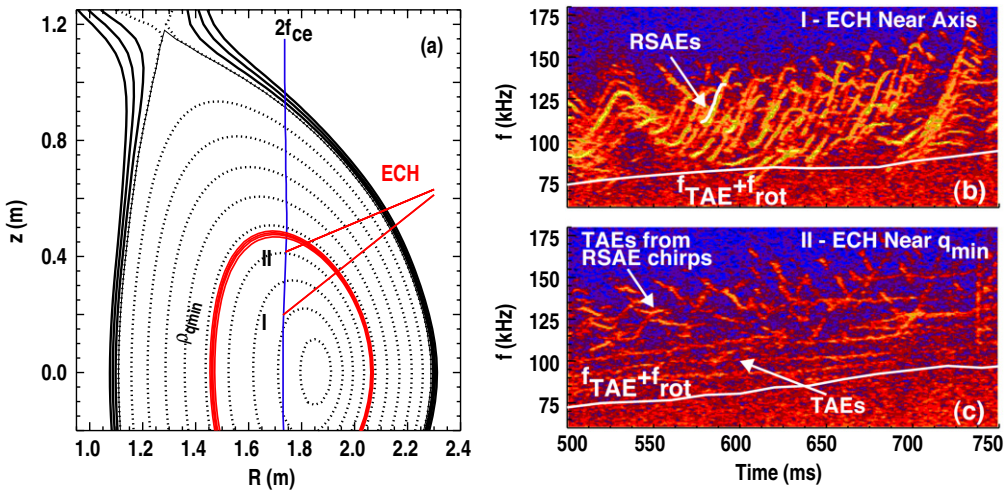

Figure 10. (*a*) Representative equilibrium overlayed with ECH ray trajectories for heating near (II) and near the axis (I). (*b*) Discharge 128564, Crosspower spectrum of vertical and radial interferometer showing RSAE activity during ECH deposition near axis. Typical RSAE frequency evolution highlighted at $t \sim 550$ ms. (*c*) Discharge 128560, Spectrum showing lack of RSAE activity during ECH deposition near $q_{\min}$. Same colour scale is used for (*b*) and (*c*).

used for figures 3 and 8. The two trajectories are initialized on the plasma outer midplane with radial positions at $q_{\min}$ (blue) and near the mode peak (white), the guiding centre of both trajectories exhibit large displacements from the flux surfaces. In fact, the particle initialized near $q_{\min}$ ($\rho \approx 0.45$) actually travels inside of $\rho = 0.2$ and fairly close to the magnetic axis on the high field side. Mathematically, the poloidal drift motion can be expanded in Fourier harmonics of the poloidal angle and the Fourier amplitude of a given harmonic is directly related to the higher order resonance drive.

This dominance of higher order resonances is something that must be considered in reversed magnetic shear plasmas such as those in advanced tokamak plasmas as well as in burning plasmas where high-n instabilities are expected. In addition to enhancing mode drive, these large orbit deviations also increase the ability of modes localized far from the magnetic axis to actually cause enhanced central fast ion transport.

3. ECH stabilization of RSAEs and impact on fast ion transport

Interestingly, the use of ECH in a set of experiments designed to probe the RSAE dependence on finite pressure effects resulted in the almost complete stabilization of RSAEs and a significant effect on the observed fast ion transport [11]. The discharge used in this experiment was very similar to 122117 discussed in the previous sections. The major difference is that during the current rise phase, approximately 1.9 MW of 110 GHz ECH power was injected radially to heat electrons and minimize net current drive. Both ECH and NBI injection begin at $t = 300$ ms and remain on throughout the current ramp phase. A typical equilibrium magnetic flux surface reconstruction overlayed with two of the ray trajectories used in the experiment is shown in figure 10(*a*). The ray trajectories do not include refraction so the actual deposition location at the second electron cyclotron harmonic layer ($2f_{ce}$) was at slightly larger minor radius. The trajectory marked II terminates near the shear reversal point ($\rho_{q\min}$) and that marked I is closer to the magnetic axis.

The suppression of RSAE activity when ECH is deposited near $q_{\min}$ is shown in figure 10(*b*) and (*c*), where crosspower spectra of vertical and radial CO_2 interferometer chords are shown. Each of these spectra show a variety of AEs typical for this type of discharge and similar to that shown for discharge 122117 in figure 1. The primary difference between these discharges is the dramatic lack of RSAE activity for ECH deposition near $q_{\min}$ (figure 10(*c*)). In figure 10(*c*) only the very end of RSAE chirps are visible where the RSAEs transition to TAEs. The combined local TAE frequency and toroidal rotation frequency near $q_{\min}$ is overlayed as well as a typical RSAE frequency sweep highlighted in figure 10(*b*). The overplotted ($f_{\rm TAE} + f_{\rm rot}$) represents the approximate frequency of an $n = 1$ TAE near $q_{\min}$. The majority of the TAEs shown are $n > 1$ and will be Doppler shifted to larger frequencies given approximately by $f_{\rm TAE} + nf_{\rm rot}$. The modes sweeping up in frequency on the timescale of 10–20 ms are RSAEs and the relatively constant frequency modes are global TAEs or the TAEs resulting from the RSAE to TAE transition. Cursory analysis of ECE data shows that several of the RSAEs in figure 10(*b*) are actually higher radial harmonics such as those presented in figures 4 and 5. Other low level TAEs have emerged for the case of ECH deposition near $q_{\min}$ and are seen as a series of modes with slowly varying frequencies in the range just above the overplotted TAE frequency [11].

There is evidence for improved beam ion confinement in the discharges with ECH deposition near $q_{\min}$ and stabilized RSAEs. As a measure of the level of Alfvénic activity, figure 11(*a*) shows the temporal evolution of the integrated power in the TAE/RSAE range (50–230 kHz) of the CO_2 interferometer data presented in figure 10. Figure 11(*b*) shows the relative impact on volume averaged neutron production ($S_{\rm n}$) compared with TRANSP simulations. The discharge with ECH deposition near $q_{\min}$ and stabilized RSAE activity has higher $S_{\rm n}$ relative to the discharge with significant RSAE activity. This increased neutron emission when scaled to

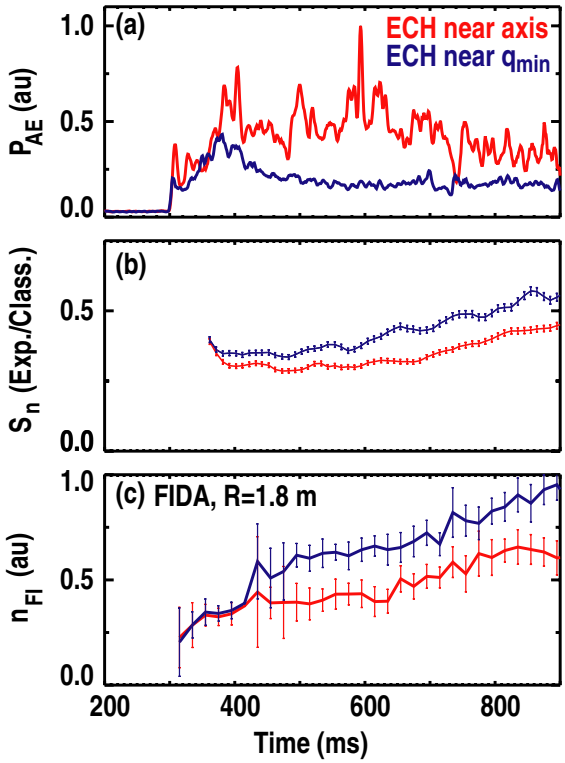

Figure 11. (*a*) Bandpass filtered (50–230 kHz) crosspower spectrum from figure 10 for deposition near magnetic axis (red) and near $q_{\min}$ (blue), a measure of AE amplitude. (*b*) Volume averaged neutron emission scaled to TRANSP predictions. (*c*) Central fast ion density measured by FIDA.

TRANSP predictions can only be due to reduced fast ion transport. An interesting point however, is that up to 60% of the reduction remains, indicating that the bulk of the neutron deficit is not due to RSAE activity in these discharges.

Further evidence of improved fast ion confinement when the RSAEs are suppressed, is given in figure 11(*c*), which shows fast ion D_α (FIDA) measurements of the density of high-energy beam ions ($n_{\rm FI}$) near the magnetic axis. Here $n_{\rm FI}$ is represented by the integrated FIDA emission in a wavelength band corresponding to energies of 30–60 keV divided by the local neutral density giving a 'FIDA Density'. Temporally, a comparison with the AE amplitude in figure 11(*a*) shows that when the AE levels are similar, the fast ion density and neutron emission for the two different deposition locations are also similar; however, after the AE levels diverge, so do the fast ion density and neutron emission. Similar to the neutron measurements, $n_{\rm FI}$ is smallest for ECH deposition near the axis and relatively higher AE amplitude.

Radial profiles of the FIDA data are given in figure 12 to show that this trend is consistent across the entire profile [13]. In terms of fast ion density, this difference is in contrast to what one would expect based purely on neutral beam ions slowing down classically due to electron drag. With the higher central $T_{\rm e}$ for ECH deposition near the axis, one would expect larger fast ion density on axis. This is clearly not the case and the increased fast ion density on axis for ECH deposition near $q_{\min}$ is attributed to reduced fast ion radial transport in the discharges with little or no RSAE [11, 13].

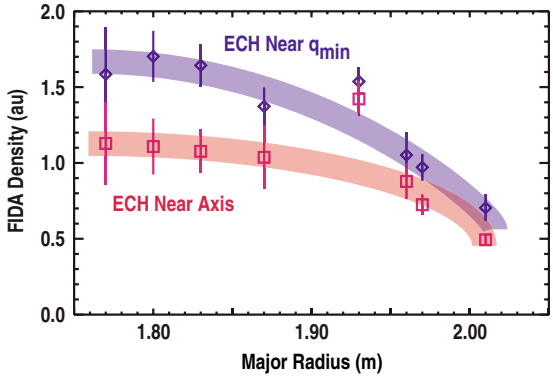

Figure 12. FIDA data for discharges in figures 10 and 11 averaged over interval $t = 500$–600 ms. Wavelength range integrated over corresponds to $E_\lambda = 30$–60 keV. Blue diamonds = ECH near $q_{\min}$, red squares = ECH near magnetic axis.

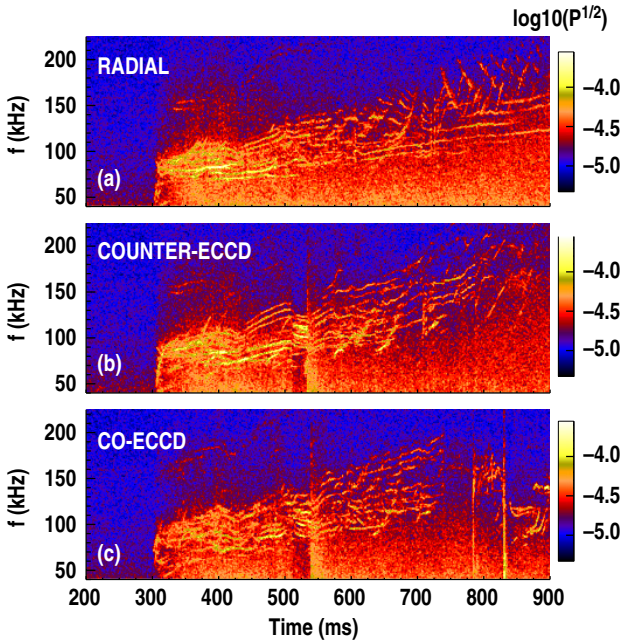

Figure 13. Crosspower spectra of vertical and radial interferometer during ECH deposition near $q_{\min}$ with (*a*) radial launch, (*b*) counter-current launch, (*c*) co-current launch.

3.1. Sensitivity of RSAE suppression to current drive phasing and ECH power

One question that arises is what effect would some amount of EC current drive have on the RSAE stabilization. To test this question, essentially the same discharge as that shown in figure 11(*c*) was repeated for purely radial, counter-current and co-current launch with EC deposition near $q_{\min}$. The co and counter phasings were intended to drive maximum co and counter current, while the radial launch was intended to purely heat. The results of this test are shown in figure 13(*a*)–(*c*) for radial, counter and co-phasing respectively. One observation that is immediately apparent from these figures is the lack of RSAE activity in all cases until very weak RSAEs appear after approximately $t = 700$ ms in the radial launch case. Also apparent is that all discharges have prominent relatively constant frequency modes which are TAEs. The

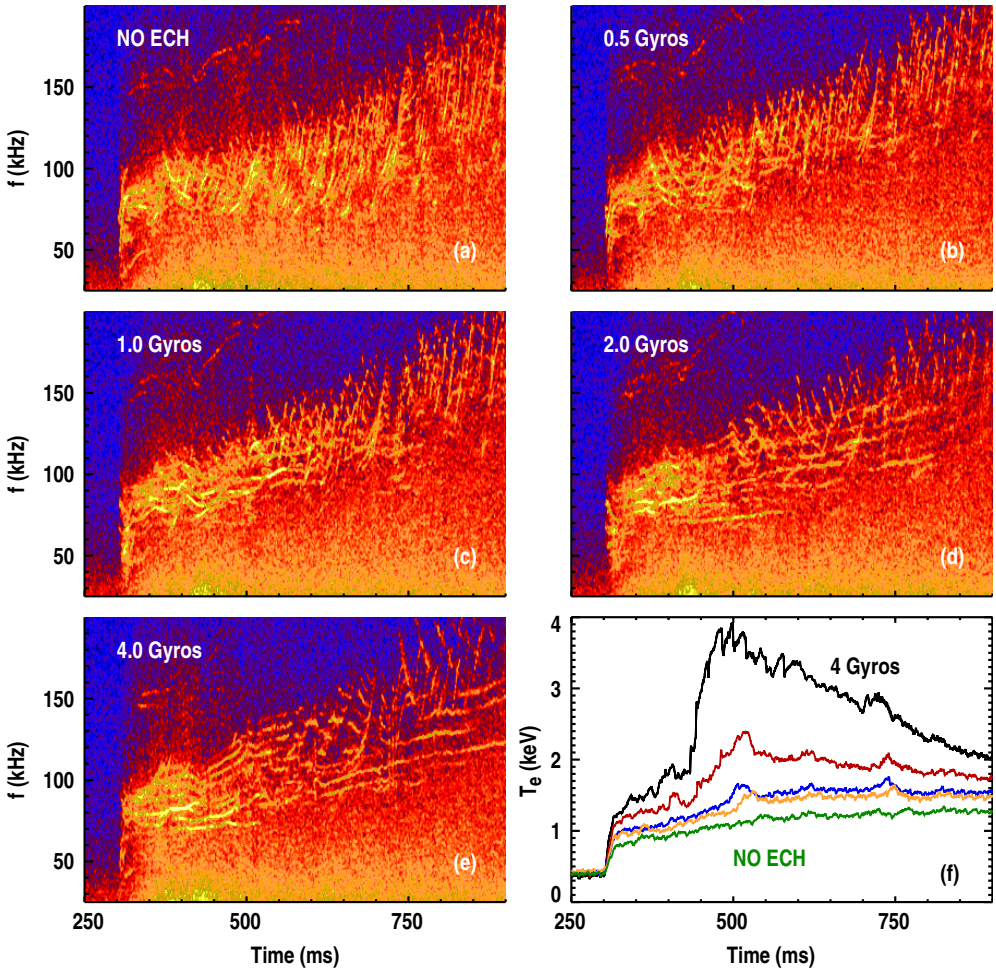

Figure 14. (*a*)–(*e*) Crosspower spectra of vertical and radial interferometer during ECH power scan with injection near q_{min}. (*a*) No ECH, (*b*) 0.5 gyrotrons, (*c*) 1.0 gyrotron, (*d*) 2.0 gyrotrons, (*e*) 4.0 gyrotrons. (*f*) Electron temperature near q_{min} (mid-radius) for cases (*a*)–(*e*).

other interesting fact is that both of the current drive phasings are essentially lacking the tops of the RSAE chirps so prominent in figure 11(*c*) and again in figure 13(*a*). Further, for both current drive phasings, a burst of intense TAEs occurs around $t = 500$ ms that does not occur for the radial launch. Interestingly, this time corresponds very nearly to where q_{min} undergoes an integer crossing ($q_{min} = 4$).

To address the question of how the RSAE stabilization depends on heating power a power scan was performed in a series of discharges by varying the number of gyrotrons used. The results of the power scan are presented in figure 14, where 0, 0.5, 1.0, 2.0 and 4.0 gyrotrons were used with 0.5 gyrotrons indicating 50% modulation at 300 Hz of a single gyrotron. Each gyrotron injects approximately 0.6 MW of RF power (on average) with the deposition intended to be near q_{min}. These data trace out a clear progression from a discharge dominated by RSAEs (No ECH, figure 14(*a*)) to a discharge dominated by TAEs (4.0 Gyrotrons, figure 14(*e*)). The actual impact on the electron temperature for the five different scenarios is shown in figure 14(*f*), where T_e is given at mid-radius near q_{min}.

The progression appears to be that the minimum frequency at which RSAEs are observed is slowly increased through the addition of heating. Also, TAEs begin to appear at higher frequencies, first for shorter duration, then at lower frequencies and finally with a duration spanning the entire time window shown. As discussed in several references, and the original motivation for this study, the RSAE is strongly affected by finite pressure—particularly near the bottom of its frequency sweep, [11, 23, 35–38]. This surely plays a role here, however, evaluation of the local GAM frequency as an estimate for the minimum RSAE frequency based on T_e and T_i at q_{min} failed to account for the entire sweep reduction [11, 39]. Further, this certainly cannot account for the difference between ECH heating near q_{min} and ECH near the axis as in figure 10, where the local temperatures are similar yet the frequency sweep range is dramatically different—this will be touched on again when discussing figure 16.

3.2. ECH modulation

Having experimentally observed that ECH near q_{min}, even at modest power levels, can significantly alter the RSAE behaviour, the natural follow on experiment is to attempt a modulation of this effect. This was attempted using four gyrotrons steered towards q_{min} as in figure 14(*e*) except with a modulation of the injected power. The modulation was carried out at two different rates, approximately 100 ms on/off and 15 ms on/off. The reason for this choice was to separate effects

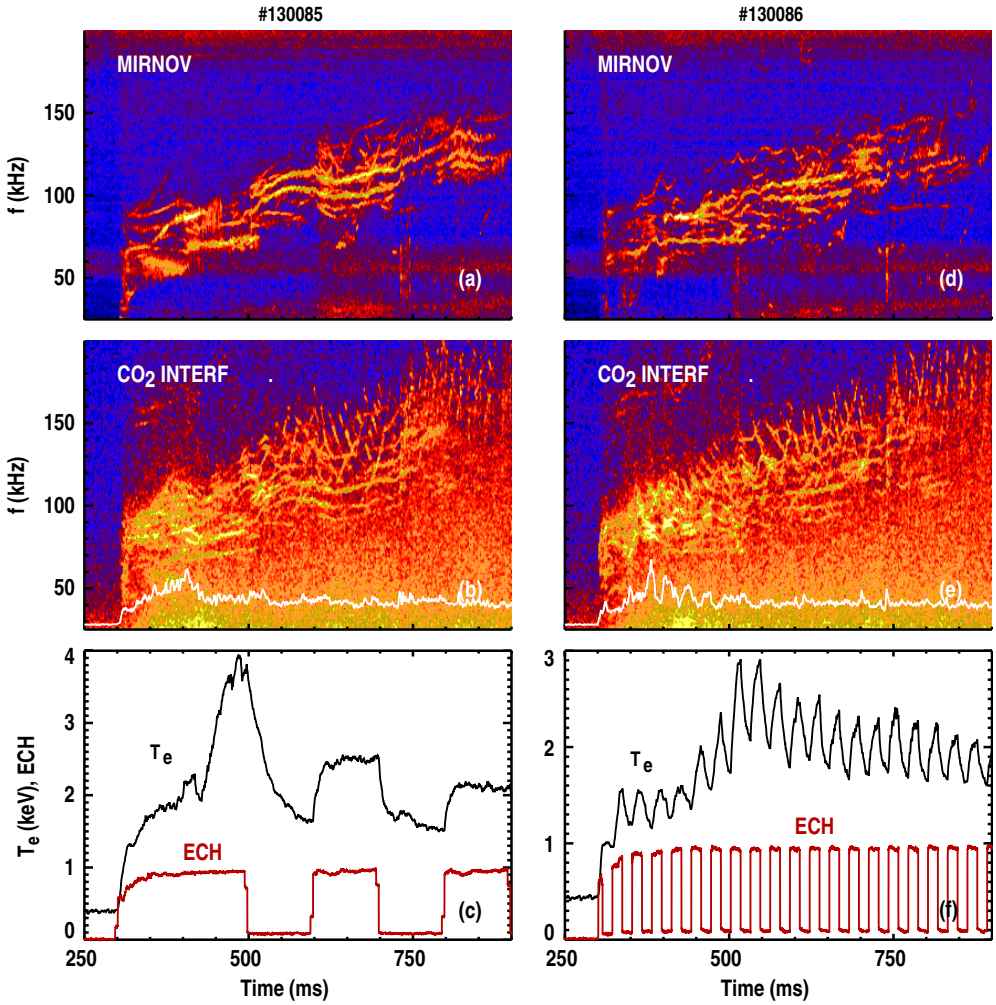

Figure 15. Data during ECH modulation with injection of four gyrotrons near $q_{\min}$. (*a*) Mirnov coil magnetic fluctuation power spectrum for ECH modulation cycle shown in (*c*). (*b*) Crosspower spectra of vertical and radial interferometer for ECH modulation cycle shown in (*c*), overplotted white curve is integrated power between 30–200 kHz. (*c*) ECH modulation waveform for 100 ms on/off. T_e near $q_{\min}$. (*d*) Mirnov coil magnetic fluctuation power spectrum for ECH modulation cycle shown in (*f*). (*e*) Crosspower spectra of vertical and radial interferometer for ECH modulation cycle shown in (*f*), overplotted white curve is integrated power between 30–200 kHz. (*f*) ECH modulation waveform for 15 ms on/off. T_e near $q_{\min}$.

that occur on a timescale slower and faster than a typical fast ion slowing down time of $\tau \approx 80$ ms.

The results of this experiment are shown in figures 15(*a*)–(*c*) and figures 15(*d*)–(*f*) for 100 ms and 15 ms modulation respectively. The gyrotron modulation waveforms and effect on T_e near $q_{\min}$ are shown in figures 15(*c*) and (*f*), while magnetic fluctuation data are shown in panels 15(*a*) and (*d*) and density fluctuation data from interferometery in panels 15(*b*) and (*e*). In each case, the electron temperature shows a clear modulation synced with the ECH as expected. Surprisingly, however, the RSAE activity (or lack of) does not show a similar modulation in either case. In both cases, the RSAEs are largely suppressed as in figure 14. This is an important piece of information in that it tells one the suppression mechanism is not related to a direct interaction with the RF wave. Also, it is likely that the RSAE stabilization is not a result of enhanced electron collisional damping due to an increased population of trapped electrons near the trapped/passing boundary during heating, as was suggested to be a possibility in [11]. This effect would also be clearly modulated with the injected ECH. It should be pointed out that the modulated electron temperature at $q_{\min}$ never relaxes back to that observed for no ECH heating as in figure 14(*c*), however, it is close at later times for 100 ms modulation when RSAEs still have not re-appeared.

Interestingly, other modulation of the AE activity does appear to occur. This modulation is most apparent for the 100 ms modulation by looking at the Mirnov data presented in figure 15(*a*) where it is clearly observed that some TAEs appear to be modulated in frequency at the ECH modulation period as well as in amplitude such as near the turn-on of the $t = 600$ ms pulse. The 15 ms modulation Mirnov data clearly show modulation of a higher frequency TAE at the ECH modulation period and the CO_2 interferometer data in figure 15(*e*) show large amplitude oscillations of the TAE amplitudes at the ECH modulation frequency. To further convey this point, the integrated power of CO_2 interferometer data in the AE band is displayed in figures 15(*b*) and (*e*) as a white overlayed line with the zero level corresponding to $t < 300$ ms. Here, a clear modulation out of phase with the injected ECH power is seen for the 15 ms modulation

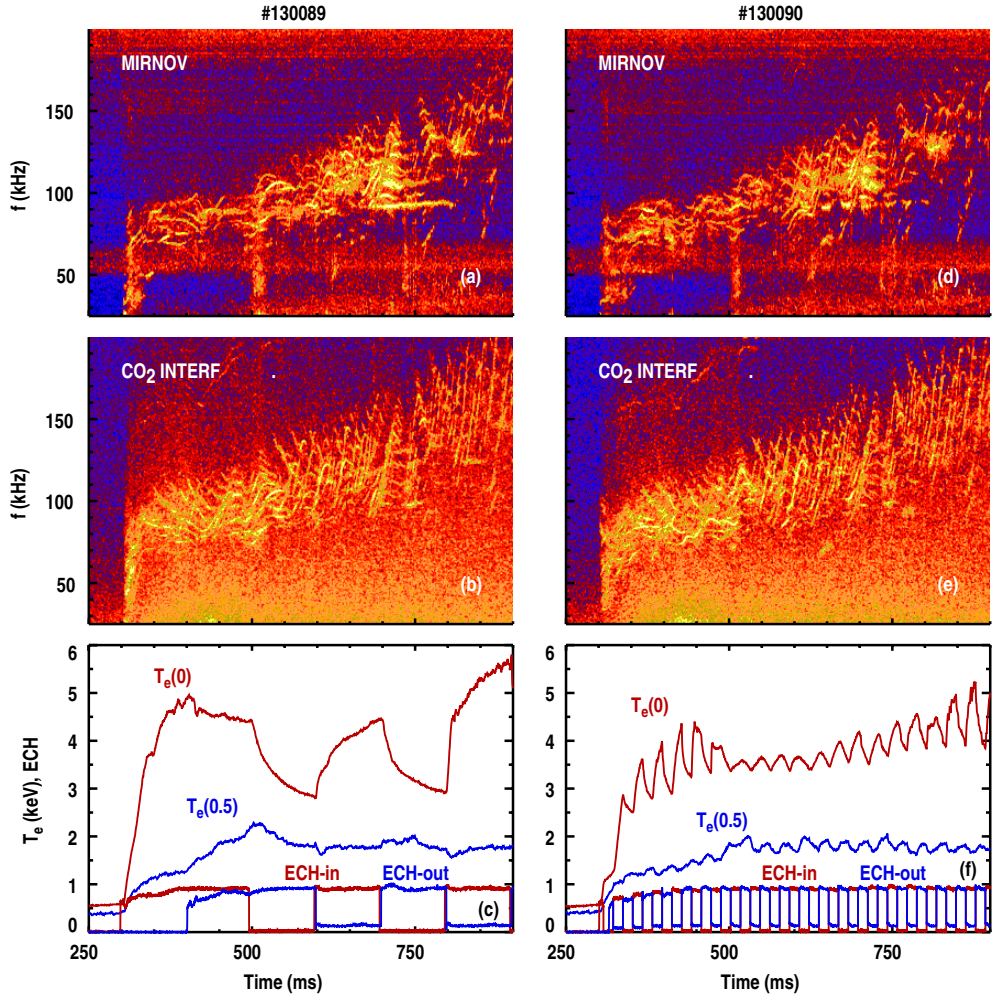

Figure 16. Data during ECH modulation with injection of two gyrotrons near $q_{\min}$ and two gyrotrons near magnetic axis. (*a*) Mirnov coil magnetic fluctuation power spectrum for ECH modulation cycle shown in (*c*). (*b*) Crosspower spectra of vertical and radial interferometer for ECH modulation cycle shown in (*c*). (*c*) ECH modulation waveforms for 100 ms on/off, blue = near $q_{\min}$, red = near magnetic axis. Blue $T_e(0.5)$ = electron temperature near $q_{\min}$ (mid-radius), red $T_e(0)$ = electron temperature near magnetic axis. (*d*) Mirnov coil magnetic fluctuation power spectrum for ECH modulation cycle shown in (*f*). (*e*) Crosspower spectra of vertical and radial interferometer for ECH modulation cycle shown in (*f*). (*f*) ECH modulation waveforms for 15 ms on/off, blue = near $q_{\min}$, red = near magnetic axis. Blue $T_e(0.5)$ = electron temperature near $q_{\min}$ (mid-radius), red $T_e(0)$ = electron temperature near magnetic axis.

period. In fact, the integrated power is changing by a factor of almost two at each ECH pulse before $t = 500$ ms. This is consistent with the ECH reducing the overall level of AE activity when deposited near $q_{\min}$. The fact that this AE amplitude modulation is able to occur on a timescale much faster than the fast ion slowing down time points to some effect other than a modification of the fast ion distribution function as the stabilizing mechanism.

As shown in the beginning of section 3, for ECH deposition near the magnetic axis strong RSAE activity was observed (figure 10(*b*)), while all of the subsequent figures have shown ECH deposition near $q_{\min}$ suppressing RSAE activity. A logical combination of these two observations is to alternate between ECH deposition at $q_{\min}$ and near the magnetic axis in the same discharge to see if one is able to switch between AE activity dominated by TAEs and RSAEs respectively. This experiment was carried out with two gyrotrons steered to each trajectory shown in figure 10(*a*), where each set was modulated out of phase with the other. The modulation period was again varied from 100 ms on/off to 15 ms on/off and the respective waveforms are shown in figures 16(*c*) and (*f*), where the local T_e is also shown near the magnetic axis (red) and near $q_{\min}$ (blue). Again, the surprising result was found that no modulation of the RSAE activity occurred for either case, however, this time the RSAEs were actually present, in contrast to the modulation experiment presented in figure 15. Also, it should be noted that these modes appeared despite the fact that the local electron temperature at $q_{\min}$ was near that for at least some of the conditions shown in figures 14 and 15. This combined with the fact that the RSAE frequency sweep ranges are very comparable to that shown for NO ECH in figure 14(*a*) argues that the RSAE suppression is not simply a reduction in the sweep range by an increasing GAM frequency. In fact the RSAE activity appears to be virtually unaffected by the ECH modulation in both cases. The clearest sign of mode amplitude modulation is that of the $f \approx 95$ kHz global TAE apparent on magnetic fluctuation data (figures 16(*a*) and (*d*)) that begins at $t \approx 670$ ms.

Table 1. Summary of ECH deposition variations and affect on AEs.

ECH variation	Observations and implications
CW, 4 gyros near axis	RSAEs and TAEs observed
CW, 4 gyros near q_{min}	TAEs from RSAE to TAE transition and global TAEs observed
CW, 4 gyros near q_{min}, scan co, counter, radial launch	RSAE suppression similar in all cases and prominent TAEs. Burst of strong TAE activity for co/ctr phasing near integer q_{min} crossing.
CW, 0–4 gyro power scan near q_{min}	Clear progression from discharge dominated by RSAEs (no ECH) to discharge dominated by TAEs (4 gyros). Minimum frequency RSAEs observed at increases and TAEs begin to appear first at higher frequencies for short duration (1–2 gyros) then at lower frequencies for entire time window (3–4 gyros).
Modulated 100 ms on/off and 15 ms on/off, 4 gyros near q_{min}	RSAEs suppressed in both cases—effect shows no modulation. Indicates suppression is not related to direct interaction with RF wave nor is it due to enhancement of e^- collision damping due to temporarily increased population of trapped electrons. Frequency of TAEs appears modulated in both cases—possibly due to equilibrium changes. TAE amplitude modulation occurs—is most clear for 15 ms modulation. Indicates TAE amplitude modification is not due to changes in fast ion distribution function (too fast).
Modulated 100 ms on/off and 15 ms on/off, 2 gyros near q_{min} and 2 gyros near axis modulated out of phase	RSAEs and TAEs observed in both cases—RSAEs not modulated. Similar activity to 4 gyros near axis only. Some TAEs observed to be amplitude modulated (clearly turned on and off).

4. Summary and conclusions

Significant progress has been made recently in understanding several aspects of AEs in reversed magnetic shear DIII-D plasmas. It was found that ideal MHD modelling of eigenmode spectral evolution, coupling, and structure using the NOVA code are in excellent agreement with experimental measurements. It was also found that higher radial envelope harmonic RSAEs are clearly observed and agree with modelling. Some discrepancies with NOVA modelling such as a radially sheared eigenmode phase along the device midplane due to up/down eigenmode asymmetries were also pointed out, however, this effect was found to be consistent with calculations using the TAEFL code in which up/down symmetric eigenmodes are not assumed. The prevalence of AEs during the discharge current ramp phase is found to be due to the high central safety factor and strong drive due to multiple higher order resonances.

Progress was even made towards control of these instabilities when it was empirically observed that ECH, when applied near the shear reversal point, could be used to effectively target and suppress RSAEs with a significant impact on fast ion confinement. The sensitivity of this effect to deposition power and current drive phasing as well as ECH modulation were also explored and a summary of the results are presented in table 1. Currently, the actual RSAE stabilization mechanism is not known, however these experiments show that in principle ECH provides a powerful tool for selectively controlling or altering AE behaviour.

Acknowledgments

This work was supported by the US Department of Energy under DE-FC02-04ER54698, SC-G903402, DE-ACC02-76CH03073, DE-FG03-07ER54415, DE-AC52-07NA27344, DE-FG02-89ER53296 and DE-AC05-00OR22725.

References

[1] Fu G.Y. and Van Dam J.W. 1989 *Phys. Fluids* B **1** 1949
[2] Wong K.L., Budny R., Nazikian R., Petty C.C., Greenfield C.M., Heidbrink W.W. and Ruskov E. 2004 *Phys. Rev. Lett.* **93** 085002-1
[3] Zonca F. *et al* 2004 *Nucl. Fusion* **45** 477
[4] Munoz M. *et al* 2008 *Phys. Rev. Lett.* **100** 055005
[5] Kramer G.J., Cheng C.Z., Fu G.Y., Kusama Y., Nazikian R., Ozeki T. and Tobita K. 1999 *Phys. Rev. Lett.* **83** 2961
[6] Van Zeeland M.A., Austin M.E., Gorelenkov N.N., Heidbrink W.W., Kramer G.J., Makowski M.A., McKee G.R., Nazikian R., Ruskov E. and Turnbull A.D. 2007 *Phys. Plasmas* **14** 056102
[7] Nazikian R. *et al* 2008 *Phys. Plasmas* **15** 056107
[8] Nazikian R. *et al* 2006 *Phys. Rev. Lett.* **96** 105006
[9] Van Zeeland M.A., Kramer G.J., Austin M.E., Boivin R.L., Heidbrink W.W., Makowski M.A., McKee G.R., Nazikian R., Solomon W.M. and Wang G. 2006 *Phys. Rev. Lett.* **97** 135001
[10] Kusama Y. *et al* 1998 *Nucl. Fusion* **38** 1215
[11] Van Zeeland M.A. *et al* 2008 *Plasma Phys. Control. Fusion* **50** 035009
[12] Heidbrink W.W. *et al* 2007 *Phys. Rev. Lett.* **99** 245002-1
[13] Heidbrink W.W. *et al* 2008 *Nucl. Fusion* **48** 084001
[14] Budny R.V. 1994 *Nucl. Fusion* **34** 1247
[15] Van Zeeland M.A., Kramer G.J., Nazikian R., Berk H.L., Carlstrom T.N. and Solomon W.M. 2005 *Plasma Phys. Control. Fusion* **47** L31
[16] Sharapov S.E. *et al* 2004 *Phys. Rev. Lett.* **93** 165001
[17] Nave M.F. *et al* 2004 *Rev. Sci. Instrum.* **75** 4274
[18] Takechi M. *et al* 2005 *Phys. Plasmas* **12** 082509
[19] Van Zeeland M.A. *et al* 2006 *Nucl. Fusion* **46** S880
[20] Holcomb C.T., Makowski M.A., Jayakumar R.J., Allen S.A., Ellis R.M., Geer R., Behne D., Morris K.L., Seppala L.G. and Moller J.M. 2006 *Rev. Sci. Instrum.* **77** 10E506
[21] Cheng C.Z. and Chance M.S. 1987 *J. Comput. Phys.* **71** 124
[22] Cheng C.Z. 1992 *Phys. Rep.* **211** 1
[23] Gorelenkov N.N., Kramer G.J. and Nazikian R. 2006 *Plasma Phys. Control. Fusion* **48** 1255
[24] Sharapov S.E. *et al* 2002 *Phys. Plasmas* **9** 2027
[25] Ferron J.R. and Strait E.J. 1992 *Rev. Sci. Instrum.* **63** 4799
[26] Briguglio S. *et al* 1998 *Phys. Plasmas* **5** 3287
[27] Spong D.A., Carreras B.A. and Hedrick C.L. 1992 *Phys. Fluids* B **4** 3316

[28] Spong D.A., Carreras B.A. and Hedrick C.L. 1994 *Phys. Plasmas* **1** 1503
[29] Lao L.L., St John H.E., Stambaugh R.D., Kellman A.G. and Pfeiffer W. 1985 *Nucl. Fusion* **25** 1611
[30] Gorelenkov N.N., Cheng C.Z. and Fu G.Y. 1999 *Phys. Plasmas* **6** 2802
[31] Gorelenkov N.N., Berk H.L. and Budny R. 2005 *Nucl. Fusion* **45** 226
[32] Pinches S.D. *et al* 2006 *Nucl. Fusion* **46** S904
[33] Todo Y. and Sato T. 1998 *Phys. Plasmas* **5** 1321
[34] Heidbrink W.W. 2008 *Phys. Plasmas* **15** 055501
[35] Kramer G.J., Gorelenkov N.N., Nazikian R.M. and Cheng C.Z. 2004 *Plasma Phys. Control. Fusion* **46** L23
[36] Breizman B.N., Parker M.S. and Sharapov S.E. 2006 *Phys. Plasmas* **12** 112506
[37] Chu M.S., Greene J.M., Lao L.L., Turnbull A.D. and Chance M.S. 1992 *Phys. Fluids* B **4** 3713
[38] Fu G.Y. and Berk H.L. 2006 *Phys. Plasmas* **13** 052502
[39] Fredrickson E.D., Crocker N.A., Gorelenkov N.N., Heidbrink W.W., Kubota S., Levinton F.M., Yuh H., Menard J.E. and Bell R.E. 2007 *Phys. Plasmas* **14** 102510